An Inverse Finite Element Approach for Estimating the Fiber Orientations in Intercostal Muscles

Mohsin Hamzah, Damien Subit, Sourabh Boruah, Jason Forman, Jeff Crandall, Daisuke Ito, Susumu Ejima , Koichi Kamiji, and Tsuyoshi Yasuki

Abstract The prediction of rib fractures using a computational thorax model remains an important and elusive challenge. The finite element models currently available do not properly include the contribution of the intercostal muscles (ICM). The mechanical behavior of these muscles, which are composed of several layers with their own fiber orientations, is not sufficiently known yet. However, documenting the orientation of the muscle fibers in each layer is not trivial. Therefore, the goal of this study was to evaluate whether the addition of the fiber orientations in a constitutive model of the ICM would improve the prediction of the ICM mechanical response. To do so, tensile tests were performed on three ICM samples harvested from one cadaver. After preconditioning, the samples were tested to fracture under quasi-static loading. The load and applied displacement were measured, and an optical system (ARAMIS) was used to measure the strain field on the external layer. Material parameters and the fiber orientations were estimated through an optimization process and an inverse FE approach, where the experimental stress–strain profiles were fitted to those obtained from the FE simulations performed specifically for the samples. The prediction of the ICM mechanical response improved when proper fiber orientation was taken into account.

Keywords anisotropic hyperelastic materials, fiber orientations, intercostal muscles, inverse finite element, tensile tests, experiment, image correlation

I. INTRODUCTION

The prediction of rib fractures using a computational thorax model remains an important and elusive challenge, as the finite element (FE) models currently available generally fail to match both the number and the location of the fractures reported during experimental tests. Although a large body of research dealing with thorax injury tolerance exists, the available thorax FE models are still lacking in the knowledge of the contribution of the intercostal muscles (ICM). Several models have been developed to model the response of the chest or the entire body under a variety of loading conditions [1-6], based on the work performed to determine the material properties of various isolated thoracic components, including clavicles [7], ribs [8-9] and costal cartilage [10-11]. However, there is little work in the literature that describes the contribution of the intercostal muscles and no work on constitutive modeling of ICM.

Finite element modeling facilitates the simulation of thoracic impacts using a wide variety of boundary conditions, material properties and other variables that would not be possible to evaluate experimentally due to cost, material availability, instrumentation limitations or physical constraints. FE modeling of the thorax helps to improve the understanding of the injury mechanisms in the ribs, and consequently more accurate FE models that account for the contribution of each anatomical component of the thorax are expected to improve injury prediction capabilities. While the contribution of the bony structure is quite well understood in injury biomechanics, the role of soft tissue such as the ICM in the chest deformation has yet to be quantified.

The ICM are located in the intercostal space and help to expand and shrink the size of the chest cavity during breathing. They are made of three layers named external, internal and innermost layers or intercostal muscles. The internal ICM, located inside the ribcage, extend from the front of the ribs and go around the back, past the bend in the ribs. The external ICM, located outside the ribcage, wrap around from the back of the rib almost to the end of the bony part of the rib in front. The fibers in the external and internal layers are orientated diagonally with respect to the ribs and run in opposite directions (Fig. 1). ICM demonstrate a number of

M. Hamzah (mnh2n@virginia.edu), D. Subit, S. Boruah, J. Forman & J. Crandall – Center for Applied Biomechanics, University of Virginia, USA. D. Ito & S. Ejima – Japan Automotive Research Institute, Tsukuba, Japan. K. Kamiji & T. Yasuki, Japan Automobile Manufacturers Association, Tokyo, Japan.

complex features including nonlinearity, incompressibility and anisotropy that are not yet well described.

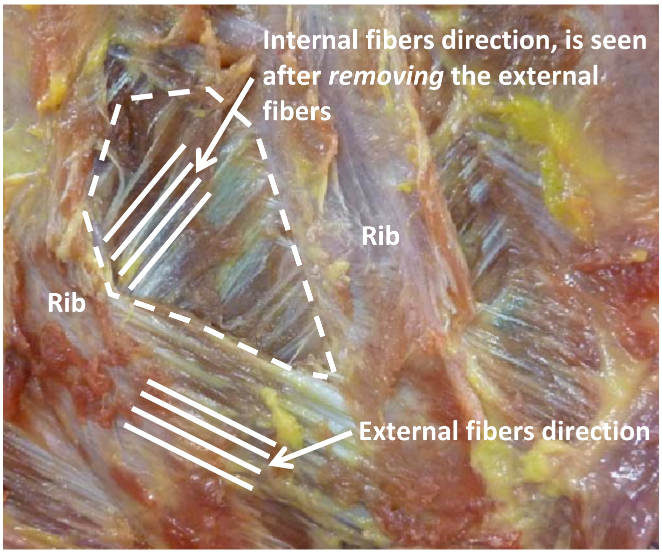

Fig. 1. Intercostal muscles fibers directions (location between ribs 5 and 6)

The goal of this paper was to introduce a novel experimental and theoretical analysis to quantify the effect of the fiber orientation on the mechanical response of the ICM. Tensile tests were performed on ICM samples harvested on one post-mortem human subject and an optical system was used to measure the strain field on the external layer. Next, a theoretical framework was outlined to develop a constitutive model of the ICM: based on an optimization scheme and an inverse FE approach, the material parameters and the fiber orientation were determined for a hyperelastic model that includes anisotropy.

II. METHODS

Experimental Testing

Three specimens of ICM were extracted from one post-mortem human subject (70 year old, 160 cm tall, 60 kg): one sample (#A) located between ribs 8 and 9 from the anterior aspect of the rib cage, and two samples (#B and #C) located between ribs 9 and 10 in the lateral and posterior aspects of the rib cage. The dimensions of the ICM specimens are detailed in Table 1. Each sample consisted of rectangles of ICM connected to the adjacent superior and inferior sections of rib, and included the entire depth of the muscle wall and the soft tissue (parietal pleura) attached to the internal surface of the ICM (Fig. 2). Prior to their excision, the two rib sections were connected to a wire of copper that maintained their relative position. Once harvested, the angle of the muscle fibers with respect to the inferior rib was measured for the internal and external layers, and the rib sections were potted in blocks (approx. 50 mm × 50 mm × 25 mm deep) of Fast Cast® casting resin (Goldenwest Manufacturing, Inc.).

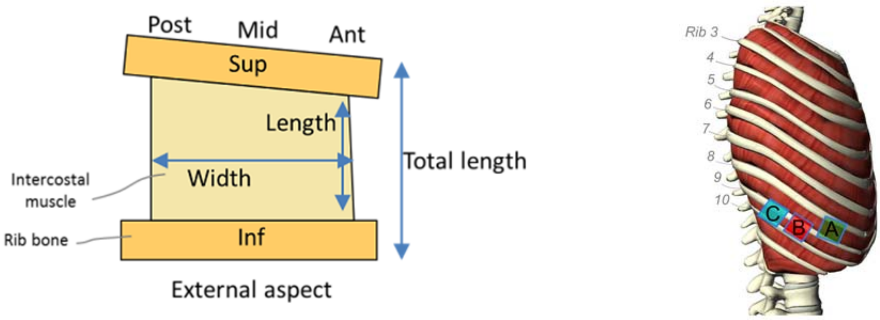

Fig. 2. Dimensions and locations of the ICM samples.

TABLE 1
DIMENSIONS OF THE ICM SPECIMENS

Sample	Total length (mm)			Muscle length (mm)		Width (mm)		Thickness (mm)	
	Ant	Mid	Post	Ant	Post	Sup	Inf	Ant	Post
A	40.0	41.6	43.4	17.1	16.3	30.0	28.0	4.3	4.7
B	50.0	52.5	53.1	21.2	19.0	28.9	28.3	2.8	2.3
C	52.2	51.6	49.3	18.1	15.3	29.0	29.0	2.5	4.4

Prior to testing, each of the specimens was soaked in body temperature (37° C) saline solution for about 2 hours to allow them to rehydrate if needed. This soaking step was shown to be effective to maintain the tissue in good condition [11], as the tests were performed in open air at room temperature. After this soaking time, each specimen was removed from the soaking solution and the surface was patted dry. The anterior surface of the specimen (i.e. the ICM outer layer) was then covered with a black and white speckle pattern (Fig. 3a). An optical system was used to measure the strain during the experiment: the deformation of the painted surface was recorded with two high-speed cameras (NAC-GX1) at 2,000 frames per second, with a resolution of 1280×1024 pixels. Prior to recording the images, the two cameras were affixed to a rigid bar, and their orientation was adjusted so that (1) the center of the field of view of each camera was confounded in the focus plane and (2) the angle between the cameras was between 15 and 25 degrees (Fig. 3b). The 2-cameras system was then calibrated so that the surface displacement and strain fields could be calculated with the ARAMIS software package (version 6.2.0, GOM-Optical Measuring Techniques, Germany).

Potted superior rib

ICM

Potted inferior rib

(a)

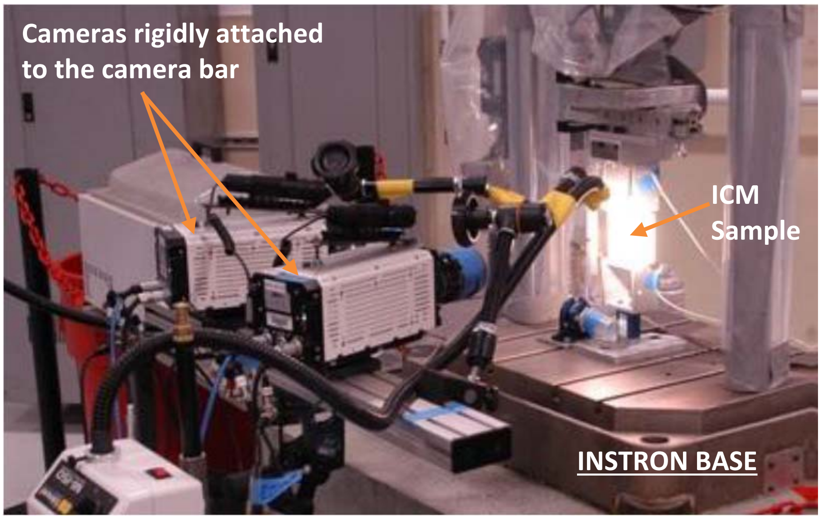

(b)

Fig. 3. Experimental testing: (a) ICM sample covered with the speckle pattern; (b) Cameras set-up with lights.

The block containing the inferior rib (inferior block) was connected to a 6-axis load cell, while the superior block was connected to the extremity of the piston of an Instron material test machine. Once the sample was in position, the copper wire was cut. Each specimen was subjected to a series of three tensile tests. First, each specimen was subjected to a pre-conditioning test imposing a 1 Hz, cyclical (sinusoidal) displacement in tension (no compression) for 20 cycles. The magnitude of the displacement was 5% of the initial length of the muscle. Afterwards, the test machine was reset to the initial (pre-test) specimen position. Then, each specimen was subjected to a tensile dynamic ramp-hold test. A displacement was applied via a 300 mm/s ramp. The magnitude of the displacement was 25% of the initial length of the specimen. After the ramp this position was held for 60 s to observe force relaxation in the specimens. Afterwards, the test machine was again reset to the initial (pre-test) specimen position. Finally, each specimen was subjected to a tensile quasi-static failure test, where a 3 mm/s displacement was applied past the point of failure of the specimen. The applied displacement and the load were recorded with a Dewetron (DEWE-2010 Series, Dewetron, Graz) data acquisition system. For the quasi-static failure tests data were collected at a rate of 10 kHz. The entire test matrix was provided for completeness; however, only the results of the quasi-static failure tests were used in the current study.

Computational Modeling

The intercostal muscles under consideration are assumed to be an anisotropic hyperelastic and continuous solid, which is described by the coordinate system $\mathbf{X}$ in undeformed state. After deformation the solid is described by the coordinate system $\mathbf{x}$. The deformation gradient, $\mathbf{F}$, is defined as $\mathbf{F} = \partial\mathbf{x}/\partial\mathbf{X}$, and the volume ratio, J, as $J = |\mathbf{F}| > 0$.

The deformation gradient can be decomposed into volumetric and distortional deformation, $\mathbf{F} = (J^{1/3})\bar{\mathbf{F}}$. Similarly, for the right Cauchy-Green tensor can be defined as:

$$\mathbf{C} = \mathbf{F}^{\mathrm{T}}\mathbf{F} = (J^{2/3})\bar{\mathbf{C}}, \qquad \bar{\mathbf{C}} = \bar{\mathbf{F}}^{\mathrm{T}}\bar{\mathbf{F}} \tag{1}$$

The Helmholtz free energy, W, is decoupled into the volumetric and isochoric parts. Furthermore, the isochoric part can be divided into an isotropic (independent of fiber orientations) and an anisotropic part:

$$W = W_{\mathrm{vol}}(J) + W_{\mathrm{iso}}(\bar{\mathrm{C}}) + W_{\mathrm{aniso}}(\bar{\mathbf{C}}, \mathbf{a}\otimes\mathbf{a}, \mathbf{g}\otimes\mathbf{g}) \tag{2}$$

where $\mathbf{a}$ and $\mathbf{g}$ are two fiber directions in the undeformed configuration (Fig. 4) that characterizes the anisotropic behavior of the material, with $|\mathbf{a}| = 1$, and $|\mathbf{g}| = 1$.

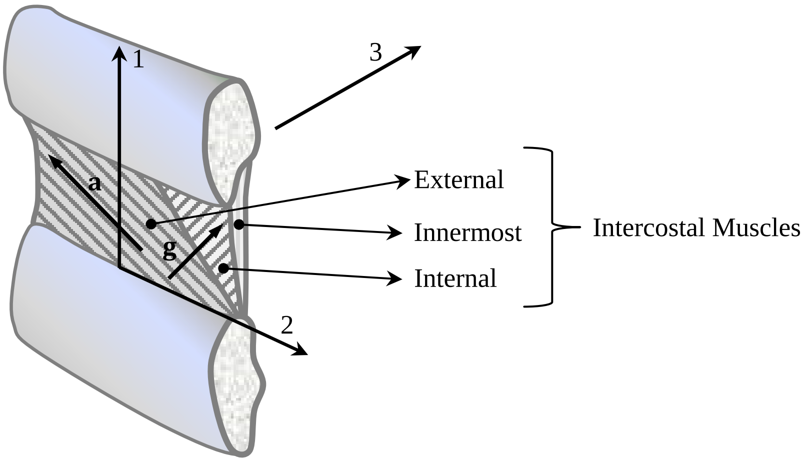

Fig. 4. Intercostal muscles layers fibers orientations

The isochoric part (isotropic and anisotropic parts) of the strain energy functions can be written in terms of strain invariants and pseudo-invariants: the isotropic part can be written in terms of the strain invariant $\bar{I}_1$and $\bar{I}_2$, while the anisotropic part can be written in terms of pseudo-invariants, which for two families of fibers are $\bar{I}_4, \bar{I}_5, \bar{I}_6, \bar{I}_7,$ and $\bar{I}_8$ [12]. In the current study, we use only $\bar{I}_4$ and $\bar{I}_6$, since they are the squares of the stretches in the directions of the fibers, and therefore have a physical interpretation [13]. The strain energy in terms of the modified invariants is:

$$W = W_{vol}(J) + W_{iso}(\bar{I}_1, \bar{I}_2) + W_{aniso}(\bar{I}_4, \bar{I}_6) \tag{3}$$

where $\bar{I}_1 = tr\,\bar{\mathbf{C}}$, $\bar{I}_2 = \frac{1}{2}\left((tr\,\bar{\mathbf{C}})^2 - \mathrm{tr}\,\bar{\mathbf{C}}^{\mathbf{2}}\right)$, $\bar{I}_4 = \mathbf{a}\cdot\bar{\mathbf{C}}\mathbf{a}$, and $\bar{I}_6 = \mathbf{g}\cdot\bar{\mathbf{C}}\mathbf{g}$.

The volumetric part of the strain energy function is given by

$$W_v(J) = \frac{1}{d}(J-1)^2 \tag{4}$$

The isotropic part of the strain energy function used in this work as a polynomial form, expressed as:

$$W_{iso}(\bar{I}_1, \bar{I}_2) = \sum_{i=1}^{3} a_i(\bar{I}_1 - 3)^i + \sum_{j=1}^{3} b_j(\bar{I}_2 - 3)^j \tag{5}$$

while the anisotropic part of the strain energy function, that is to say the energy function in the fibers, is assumed in the form of an exponential form:

$$W_{aniso}(\bar{I}_4, \bar{I}_6) = \frac{c_1}{2c_2}[\exp(c_2(\bar{I}_4 - 1)^2 - 1)] + \frac{e_1}{2e_2}[\exp(e_2(\bar{I}_6 - 1)^2 - 1)] \tag{6}$$

In order to determine the constitutive equations for anisotropic hyperelastic materials in term of strain invariants, the strain energy function, W, is differentiated with respect to the tensor $\mathbf{C}$. By means of the chain rule, the second Piola-Kirchhoff (2nd PK) stress, $\boldsymbol{S}$, can be decomposed into the volumetric and the deviatoric stresses:

$$\boldsymbol{S} = \boldsymbol{S_{vol}} + \boldsymbol{S_{iso}} + \boldsymbol{S_{aniso}} = \boldsymbol{S_{vol}} + \boldsymbol{S_{dev}} \qquad (7)$$

where $\boldsymbol{S_{vol}}$ and $\boldsymbol{S_{dev}}$ are the volumetric and the deviatoric stresses, respectively, which in turn can be expressed as:

$$\boldsymbol{S}_{\mathrm{vol}} = p\, J\, \mathbf{C}^{-1}, \qquad (8)$$

$$\boldsymbol{S_{dev}} = J^{-2/3}\left(\tilde{\mathbf{S}} - \tfrac{1}{3}\left(\bar{\mathbf{C}}:\tilde{\mathbf{S}}\right)\bar{\mathbf{C}}^{-1}\right) \qquad (9)$$

and,

$$\tilde{\mathbf{S}} = 2\frac{\partial W_{dev}}{\partial \bar{\mathbf{C}}} = 2\sum_{\alpha=1,2,4,6}^{4}\frac{\partial W_{dev}}{\partial \bar{I}_\alpha}\frac{\partial \bar{I}_\alpha}{\partial \bar{\mathbf{C}}} \qquad (10)$$

The derivatives of the modified invariants with respect to the deviatoric part of the right Cauchy-Green tensor are written as:

$$\frac{\partial \bar{I}_1}{\partial \bar{\mathbf{C}}} = \mathbf{I},\ \frac{\partial \bar{I}_2}{\partial \bar{\mathbf{C}}} = \bar{I}_1\mathbf{I} - \bar{\mathbf{C}},\ \frac{\partial \bar{I}_4}{\partial \bar{\mathbf{C}}} = \mathbf{a}\otimes\mathbf{a},\ \text{and}\ \frac{\partial \bar{I}_6}{\partial \bar{\mathbf{C}}} = \mathbf{g}\otimes\mathbf{g} \qquad (11a)$$

and the derivatives of the deviatoric part of the strain energy function with respect to the modified strain invariants are:

$$\begin{aligned}
\frac{\partial W_{dev}}{\partial \bar{I}_1} &= a_1 + 2a_2(\bar{I}_1 - 3) + 3a_3(\bar{I}_1 - 3)^2\\
\frac{\partial W_{dev}}{\partial \bar{I}_2} &= b_1 + 2b_2(\bar{I}_2 - 3) + 3b_3(\bar{I}_2 - 3)^2\\
\frac{\partial W_{dev}}{\partial \bar{I}_4} &= c_1(\bar{I}_4 - 1)\exp(c_2(\bar{I}_4 - 1)^2)\\
\frac{\partial W_{dev}}{\partial \bar{I}_6} &= e_1(\bar{I}_6 - 1)\exp(e_2(\bar{I}_6 - 1)^2)
\end{aligned} \qquad (11b)$$

The Cauchy (true) stress can be computed from the 2nd PK:

$$\boldsymbol{\sigma} = J^{-1}\mathbf{F}\,\boldsymbol{S}\,\mathbf{F}^T \qquad (12)$$

For uniaxial tension, assuming full incompressibility, i.e., J=1, $\lambda_1 = \lambda$ and, $\lambda_2 = \lambda_3 = \lambda^{-1/2}$, the deformation gradient becomes:

$$\mathbf{F} = \begin{bmatrix}\lambda & 0 & 0\\ 0 & \lambda^{-1/2} & 0\\ 0 & 0 & \lambda^{-1/2}\end{bmatrix}$$

Defining the fiber orientation vectors as $\mathbf{a} = \{\cos\beta_1, \sin\beta_1, 0\}$ and $\mathbf{g} = \{\cos\beta_2, \sin\beta_2, 0\}$, equations (11a) yields to (for uniaxial tension):

$$\frac{\partial \bar{I}_1}{\partial \bar{\mathbf{C}}} = \mathbf{I},\qquad \frac{\partial \bar{I}_2}{\partial \bar{\mathbf{C}}} = \begin{bmatrix}2\lambda^{-1} & 0 & 0\\ 0 & \lambda^2+\lambda^{-1} & 0\\ 0 & 0 & \lambda^2+\lambda^{-1}\end{bmatrix},$$

$$\frac{\partial \bar{I}_4}{\partial \bar{\mathbf{C}}} = \begin{bmatrix}\cos^2(\beta_1) & \sin(\beta_1)\cos(\beta_1) & 0\\ \sin(\beta_1)\cos(\beta_1) & \sin^2(\beta_1) & 0\\ 0 & 0 & 0\end{bmatrix},\quad \text{and}\quad \frac{\partial \bar{I}_6}{\partial \bar{\mathbf{C}}} = \begin{bmatrix}\cos^2(\beta_2) & \sin(\beta_2)\cos(\beta_2) & 0\\ \sin(\beta_2)\cos(\beta_2) & \sin^2(\beta_2) & 0\\ 0 & 0 & 0\end{bmatrix}$$

where β_1 and β_2 are the angles of the external and internal intercostal muscles fibers, respectively, measured counterclockwise from direction 1-axis (Fig. 4).

Combining the above equations with equation (7) yields to:

$$\begin{bmatrix}S_{11} & S_{12} & S_{13}\\ S_{21} & S_{22} & S_{23}\\ S_{31} & S_{32} & S_{33}\end{bmatrix} = p\begin{bmatrix}\lambda^{-2} & 0 & 0\\ 0 & \lambda & 0\\ 0 & 0 & \lambda\end{bmatrix} + \begin{bmatrix}\tilde{S}_{11} & \tilde{S}_{12} & \tilde{S}_{13}\\ \tilde{S}_{21} & \tilde{S}_{22} & \tilde{S}_{23}\\ \tilde{S}_{31} & \tilde{S}_{32} & \tilde{S}_{33}\end{bmatrix} - \frac{\lambda^2\tilde{S}_{11} + \lambda^{-1}(\tilde{S}_{22} + \tilde{S}_{33})}{3}\begin{bmatrix}\lambda^{-2} & 0 & 0\\ 0 & \lambda & 0\\ 0 & 0 & \lambda\end{bmatrix} \qquad (13)$$

Since the stresses along directions 2 and 3 (Fig 4) are zero in the case of the uniaxial test, an expression for the hydrostatic pressure can be obtained from equation (13). Then substituting the expression obtained for the hydrostatic pressure for the stress S_{11} in 1-axis yields to the following constitutive relation:

$$S_{11} = \tilde{S}_{11} - \frac{\tilde{S}_{33}}{\lambda^3} \quad (14)$$

where;

$$\tilde{S}_{11} = 2[a_1 + 2a_2(\bar{I}_1 - 3) + 3a_3(\bar{I}_1 - 3)^2] + 2[b_1 + 2b_2(\bar{I}_2 - 3) + 3b_3(\bar{I}_2 - 3)^2](2\lambda^{-1}) + 2[c_1(\bar{I}_4 - 1)\exp(c_2(\bar{I}_4 - 1)^2)]\cos^2(\beta_1) + 2[e_1(\bar{I}_6 - 1)\exp(e_2(\bar{I}_6 - 1)^2)]\cos^2(\beta_2)$$

$$\tilde{S}_{33} = 2[a_1 + 2a_2(\bar{I}_1 - 3) + 3a_3(\bar{I}_1 - 3)^2] + 2[b_1 + 2b_2(\bar{I}_2 - 3) + 3b_3(\bar{I}_2 - 3)^2](\lambda^2 + \lambda^{-1})$$

The material parameters a_1, a_2, a_3, b_1, b_2, and b_3 are related to the isotropic part of the muscles response (the matrix), while c_1, c_2, e_1, and e_2 are related to the anisotropic part (the fibers) of the response. All these parameters were estimated through an optimization process and an inverse FE approach.

Finite Element Modeling

The finite element used in the present analysis is depicted in the flowchart in Fig. 5.

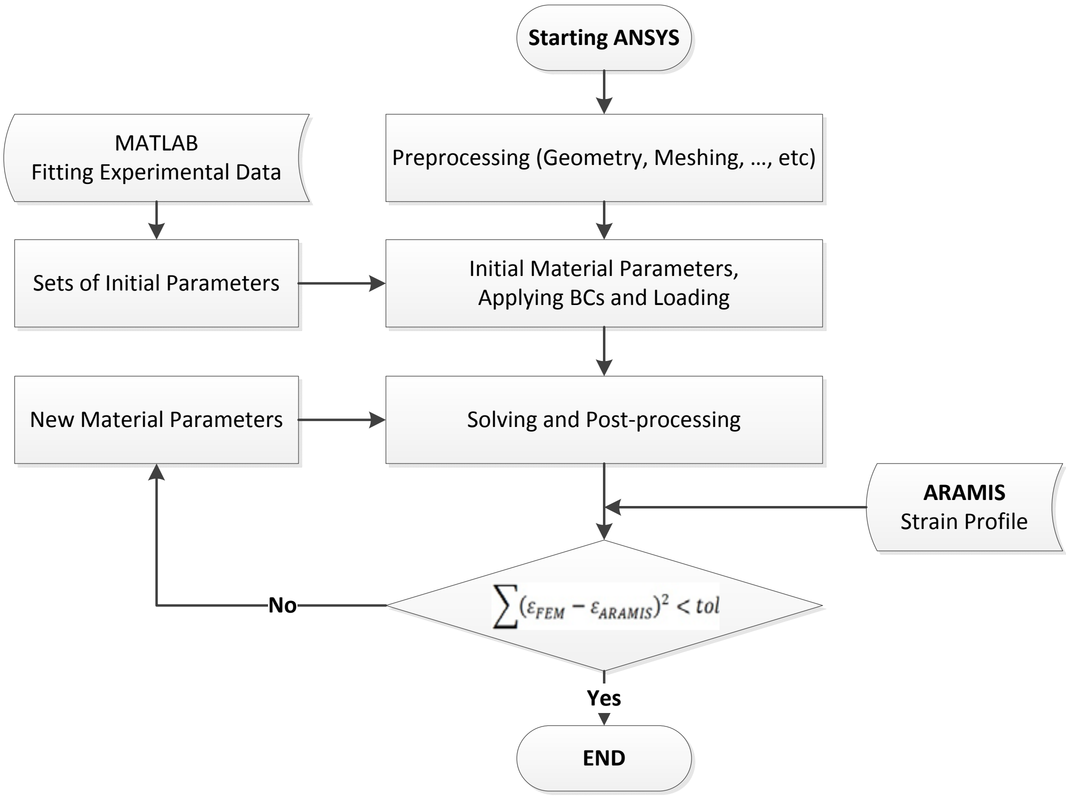

Fig. 5. Flowchart of the inverse FE analysis carried out to estimate the fiber angle in the internal layer of the ICM.

Material parameters were first adjusted using the Matlab ™ Optimization Toolbox version 7.11 (The MathWorks Inc.). The FE analysis was conducted using the ANSYS software package (ANSYS, Inc.). Once the FE model was initialized, the ANSYS Parametric Design Language (APDL) was used to perform the optimization process. The problem was solved as a 3-D solid, meshed with high order 3-D 20-node solid element with quadratic displacement interpolation (SOLID186 in ANSYS). The NLGEOM command, for nonlinear geometry solution option, was also enabled. Finally, the APDL command TB-AHYPER was invoked: this command enables the modeling of anisotropic hyperelastic materials based on the definition of a potential-based-function with parameters that define the volumetric part and the isochoric part (the matrix and the fiber directions). Once the mesh was created, the hyperelastic parameters were initialized based on the results obtained from MATLAB for different values of internal fibers angles. This analysis provided seed values for the optimization that happened next. Since the value of the internal fibers angle was unknown, the APDL script was used to build an optimization algorithm which seeks the minimum error between the strains obtained from the FE analysis at specific points on the external layer with that obtained experimentally from ARAMIS optical system to find the required internal fibers angle. This optimization consisted of changing the fiber angle and the corresponding material parameters until the error came within a certain preselected tolerance. When the tolerance was met, the optimization was terminated; otherwise, the angle and the hyperelastic parameters were updated.

As the orientation of the internal fibers was unknown in this problem, a multiple fitting of the experimental data from the uniaxial tests was implemented using the Levenberg–Marquardt algorithm to solve the nonlinear curve fitting in the least squares sense. The value of the internal fibers angle was changed in each fitting to get a set of material parameters for each angle that could be used in the FE modeling. ANSYS was used to match the strain field in specific points between FE solution and that obtained from the ARAMIS optical system. When the error comes within a certain preselected value the FE modeling gives the required internal fiber orientation angle. Since the internal layers fibers are located diagonally from the external layers, the angle of the fibers for each specimen was varied from 0° to -90° (a step of 5° was used) measured from the 1-axis in order to reduce the computational time.

Finally, in order to demonstrate the effect of the fiber orientation on the ICM response, two brief sensitivity analyses were performed. First, the contribution of anisotropy to the ICM response was evaluated by comparing the response of the FE model for Sample A obtained with an isotropic hyperelastic material model and an isotropic hyperelastic model for the ICM. Second, the variation of the stress predicted by the model as a function of the fiber orientation was assessed by quantifying the change in the model response due to a change in fiber orientation.

III. RESULTS

Tensile tests

The stress and stretch were obtained from the force and displacement: the stress was defined as the force to initial average cross-section ratio, and the stretch as the displacement to initial average length ratio using the dimensions of the samples presented in Table 1. For the three samples (Fig. 6), a toe region was observed, followed by quasi-linear response after about 30 % of stretch. The response of the ICM was location dependent, as even adjacent samples (Samples B & C) give different responses.

The strain field at the surface of the external layer was also measured for all the samples. Selective images of these results for Sample B are shown in Fig. 7: Fig. 7a and 7b show the major strains (larger principal strains) at different strain levels and the arrows in these figures indicate the direction of the major strains.

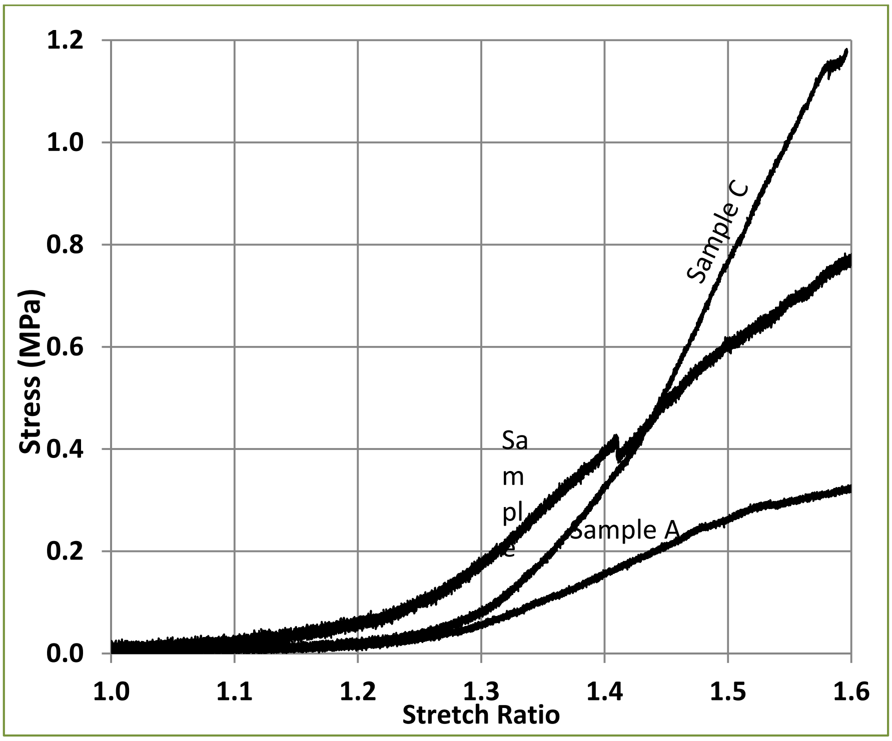

Fig. 6. Stress vs. stretch ratio for quasi-static tensile tests.

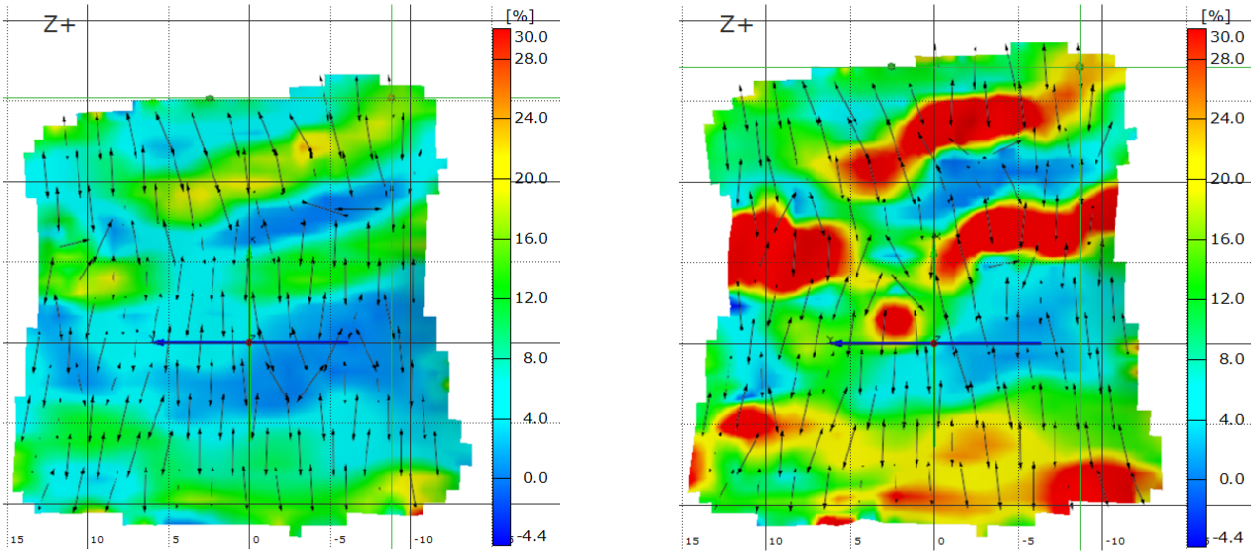

(a) (b)

Fig. 7. Sample B: (a) Major strains at 10 % strain, and (b) Major strains at 20 % strain.

Fiber orientation

The angles of the external fibers for all specimens were measured experimentally (Table 2). The fiber angle in the internal layer was estimated using the optimization procedure explained in the Methods section.

TABLE 2
ICM FIBER ANGLES FOR EXTERNAL LAYER, MEASURED FROM THE LOWER RIBS (COUNTER-CLOCKWISE)

Sample No.	Sample Between Ribs		Angle of External Layer Measured Experimentally
	Higher rib	Lower rib	
A	8	9	145°
B	9	10	147°
C	9	10	155°

In order to demonstrate the effect of the fiber orientation on the ICM response, i.e. the anisotropic behavior of the muscles, the problem was first solved for Sample A as an isotropic hyperelastic one, assuming no fibrous structure. It was observed that the strain pattern was approximately symmetrical (Fig. 8a). When anisotropy was assumed (Fig. 8b), using fiber angles of 55° for the internal layer and 145° for the external layer, the strain field was found to be unsymmetrical (Fig. 8b) . For the anisotropic solution the material parameters and fibers orientations are estimated through an optimization procedure as explained below. This demonstrates that there is a significant difference in muscle response between the two assumptions. The same conclusion is drawn for Samples B & C.

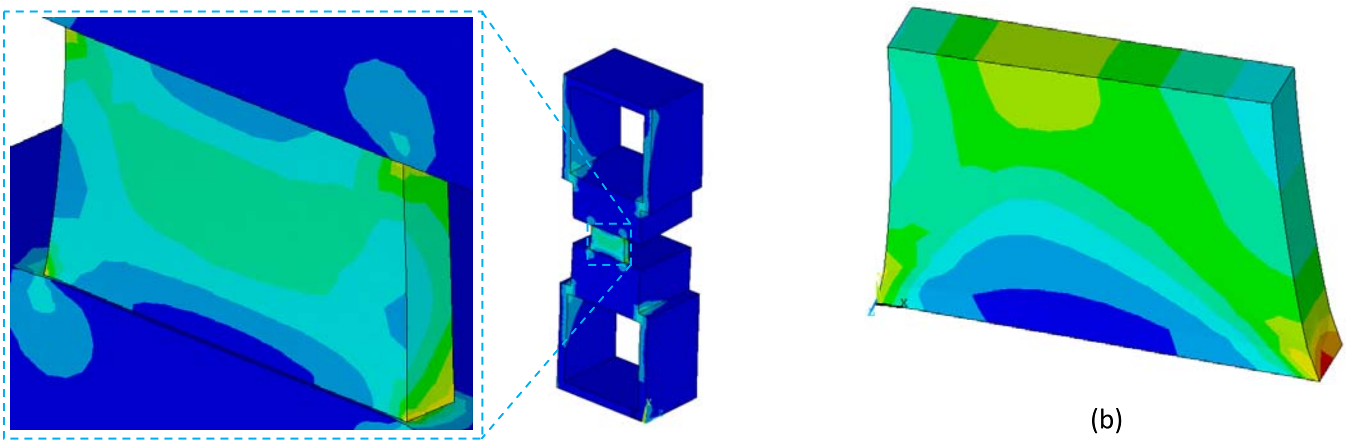

(a) (b)

Fig. 8. Effect of fiber orientations on the strain pattern in the ICM for Sample A, (a) Isotropic assumption (no fibers effect), (b) Anisotropic assumption (with fibers effect)

Determination of material parameters

The constitutive relation derived in this paper (equation 14) was used for fitting the values of the material parameters for the theoretical model presented in section II. The results of the optimization process are shown in Figures 9, 10 and 11.

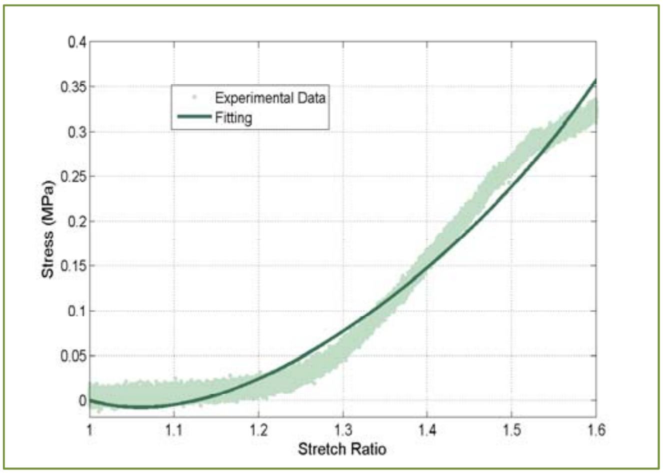

Fig. 9. Sample A curve fitting

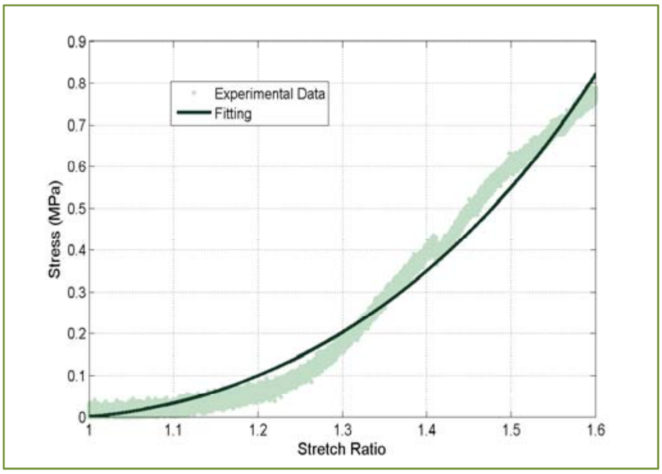

Fig. 10. Sample B curve fitting

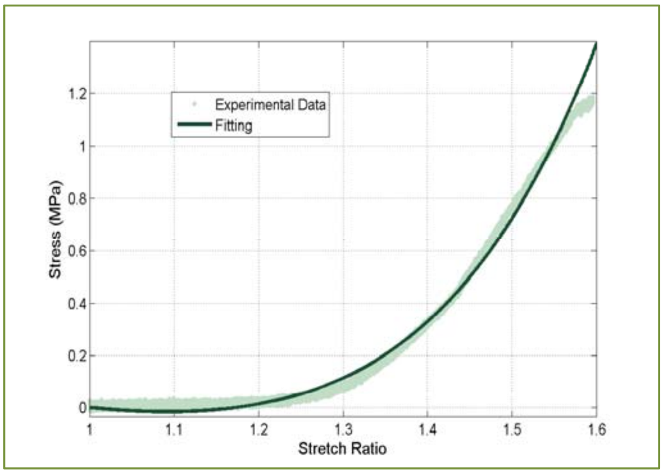

Fig. 11. Sample C curve fitting

The sensitivity of the ICM mechanical behavior to the orientation of the muscle fibers was evaluated by varying the fiber angle in the internal layer from -90 to 90° (-π/2 to π/2) relative to the 2-axis, and the fiber angle in the external layer was set to 137° and 157° (angle measured experimentally plus and minus 10°), for a strain level of 20 %.

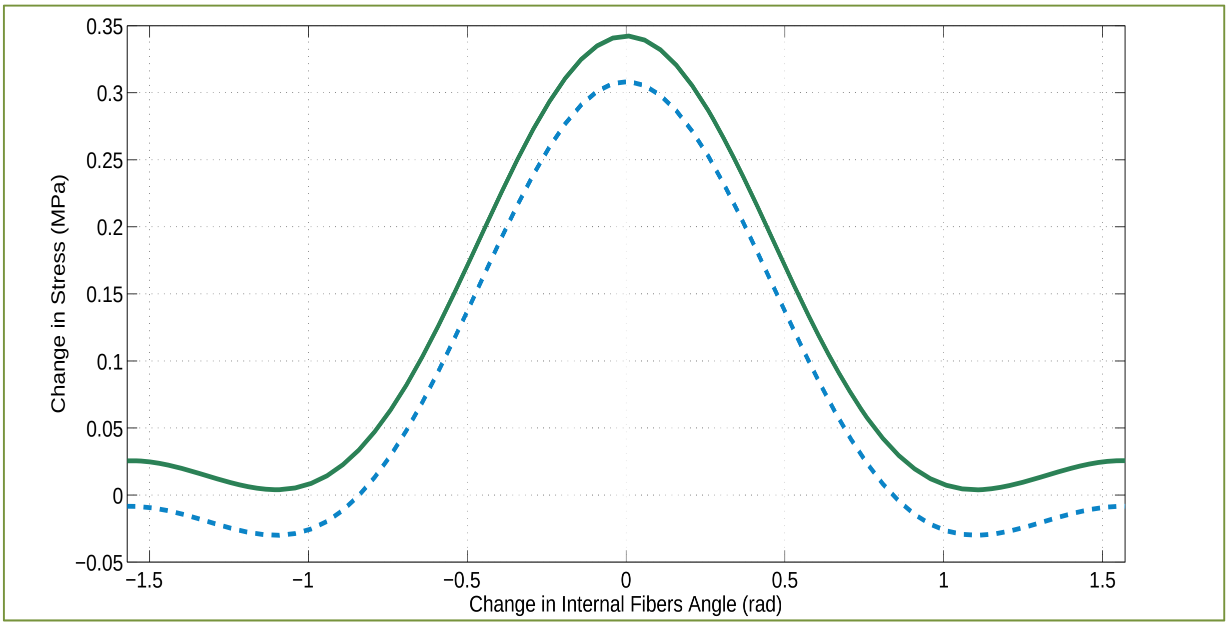

Fig. 12. Change in stress due to the change in the orientation of the fibers in the internal layer relative to the 2-axis (Sample B). Solid line: fiber angle of 137° for the external layer, dashed line: fiber angle of 157° for the external layer

The angles of the internal layer fibers obtained from the optimization procedure are summarized in Table 3. The table shows the values of the internal layer angles which were calculated using an optimization analysis for the three samples. Internal layer angles for Samples A and C were also estimated based on the optimized material parameters for Sample B.

TABLE 3
ICM FIBER ANGLES FOR INTERNAL LAYER, MEASURED FROM THE LOWER RIBS (COUNTER-CLOCKWISE)

Sample No.	Angle of External layer Measured	Angle of Internal layer Optimized from Fitting	Angle of Internal layer Estimated from material parameters obtained for Sample B
A	145°	55°	52°
B	147°	60°	60°
C	155°	70°	64°

The materials parameters obtained from the optimization process with 95% confidence bounds for the three tested ICM samples are summarized in Table 4.

TABLE 4
MATERIALS PARAMETERS OBTAINED FROM THE OPTIMIZATION PROCESS FOR THE ICM SAMPLES

Sample	Material Parameters for the ICM Samples								
	a_1	a_2	a_3	b_1	b_2	b_3	c_1 & e_1	c_2 & e_2	R^2
A	0.02001	0.01980	3.0e-14	-0.0881	0.0199	-0.1167	0.3100	0.1901	0.978
B	1.42e-6	0.02000	8.2e-14	2.3e-11	0.0198	2.2e-14	0.2885	0.1999	0.981
C	-0.0999	1.92e-6	0.1395	0.01297	6.0e-13	0.08071	0.2913	0.2002	0.995

IV. DISCUSSION

Experimental results

The ICM exhibited a common soft tissue behavior with a toe region up to approximately 20 % where little stress is generated. Samples B and C exhibited non-linearity for 1.42 and 1.57 of stretch ratios. The reasons behind these sudden drops of the stress are unclear. Two assumptions can be made. First, this could be an experimental artifact: the strain analysis relies on a speckle pattern that was created with an oil-based paint that hardens when it dries, and the drop in the stress could have been caused when the paint cracked. Indeed, because of the large deformation sustained by the ICM sample, the paint cracked in several areas when the deformation of the ICM reached the paint failure threshold. The choice of paint was a trade-off between its compliance and its ability to properly adhere to a humid surface. The second assumption is that damage occurred because of fiber decohesion or fracture. The modeling approach in the present study did not account for the damage or fracture, as this would have required to unload and load the sample several times to identify the parameters for a damage evolution law. As only three samples were tested, it is not possible to draw extensive conclusions regarding the location dependence of the ICM mechanical properties. However, it would make sense for the ICM to have location dependent properties because the mass of the thorax is not equally distributed within the ribcage.

Fiber orientation

The assumption was made that isotropy may predict the stiffness and response of the muscles when subjected to the same boundary conditions as in our experiments. Instead, it was shown that anisotropic modeling, i.e. including the contribution of the fibers, resulted in a more accurate estimate of the strain. Indeed, the strain fields in the external layer of the ICM were significantly different under these two conditions. Therefore, if isotropic behavior prevents accurately predicting the values and locations of the maximum stress during an impact, the simulation results could lead to the incorrect prediction of the number and location of the rib fractures. This could ultimately lead to a wrong estimation of the risk incurred by a belted vehicle occupant during an impact.

Material parameters

The ICM were assumed to behave as hyperelastic anisotropic and incompressible soft tissue. They were also assumed to consist of two families of fibers that were assumed to be straight. The response of the anisotropic part of the strain energy and the resultant constitutive relation was assumed to relate to the fibers only, while the isotropic part was related to an effective matrix which includes the response of the innermost layer. At low strain, the isotropic part of the muscles (the matrix material) is the effective response, and as the strain increases the stiffening of the ICM muscle occurs and the fiber response becomes the dominant response (the matrix material is significantly less stiff than the fibers). The response of the ICM was found to be location dependent, as even neighboring samples (Samples B & C) give different responses (Fig. 6). Six material parameters (a_1, a_2, a_3, b_1, b_2 and b_3) were used to describe the matrix material depending on the polynomial form of strain energy, while an exponential form of the strain energy function with two material parameters was used for each layer ($c_1,\ c_2,$ for one layer, and $e_1,\ e_2$ for the other). All these parameters were estimated through an optimization process and an inverse FE approach to estimate the angle of the internal layer fiber. The material parameters c_1 and c_2 were assumed to have the same numerical values as e_1 and e_2, respectively, and these parameters were constrained to be greater than zero to have some physical meaning (the fibers are assumed active only in extension). The fitting procedure developed in this study demonstrates the predictive ability of the current approach to estimate the anisotropic stiffening due to fiber reinforcement at large strains. The sensitivity plot presented in Fig. 12 shows that the stiffness is less sensitive to small variation of the fibers angles for both external and internal layers, but gives a totally different response for large variation of the fibers orientations. The prediction of the angles of the internal layers of Samples A & C based on material parameters of Sample B (Table 3) gives a reasonably acceptable estimation of these angles, which indicates that the fibers and matrix material properties may vary only minimally across samples. Once confirmed, this will allow a fewer number of samples to be harvested from post-mortem human subjects.

V. CONCLUSIONS

A constitutive model and an inverse FE analysis were developed to determine the anisotropic material properties of ICM. In addition to matching the stress-strain relationship, the optimization scheme constrained the computational model to match the experimental strain measured in several locations of the ICM external layer thanks to an optical strain measurement system. The optimized model was then used to evaluate the effects of the anisotropic behavior of the muscles, i.e. the effect of fibers in each layer, on the predicted mechanical behavior. The fibers orientations for the three samples were found to vary from 145° to 155° for the external layers, and from 55° to 70° for the internal layers (the angles were measured locally from the lower rib in counter-clockwise direction). The fitting procedure demonstrated the ability of the proposed model to account for the anisotropic stiffening due to fibers reinforcement at large strains.

It was shown that localization in the strain field was predicted by the computational model only when the ICM was modeled as anisotropic.

The results of the parameters optimization revealed that the ICM exhibited a high degree of anisotropy. While including fiber orientation of the ICM in a FE model of the thorax adds extra complexity to the model, the present study demonstrates that it may be a necessary step to properly match the effective stiffness of the ICM. Indeed, it is anticipated that a more accurate material model for the ICM will contribute to a better prediction of the complex strain field in the rib cage that will ultimately lead to a better understanding of the injury mechanisms.

VI. ACKNOWLEDGEMENT

Dr. Hamzah wishes to thank the Institute of International Education (IIE) and the Jefferson Scholar Foundation for their support and assistance with this project. The authors would like to acknowledge the financial support of the Japanese Automotive Research Institute (JARI) for the experimental tests.

VII. REFERENCES

[1] Lizee E, Robin S, Song E, Bertholon N, Lecoz JY, Besnault B, Lavaste F, Development of a 3D finite element model of the human body, *Proc. 42nd Stapp Car Crash Conference*, pp. 115-138, Society of Automotive Engineers, Warrendale, PA, 1998.

[2] Deng YC, Kong W, Ho H, Development of a finite element human thorax model for impact injury studies, *Society of Automotive Engineers,* Paper 1999-01-0715, Warrendale, PA, 1999.

[3] Robin S, HUMOS: Human model for safety—a joint effort towards the development of refined human-like car occupant models, *Proc. 17th Enhanced Safety of Vehicles Conference*, Paper 297, 2001.

[4] Shah CS, Yang KH, Hardy WN, Wang K, King AI, Development of a computer model to predict aortic rupture due to impact loading. *Stapp Car Crash Journal*, 45:161-182, 2001.

[5] Kimpara H, Lee J, Yang K, King A, Iwamoto M, Watanabe I, Miki K, Development of a three-dimensional finite element chest model for the 5th percentile female, *Stapp Car Crash Journal*, 49:251-269, 2005.

[6] Zhao J, Narwani G, Development of a human body finite element model for restraint system R & D application, *Proc. 19th International Technical Conference on Experimental Safety of Vehicles*, 2005.

[7] Duprey S, Bruyere K, Verriest J-P, Influence of geometrical personalization on the simulation of clavicle fractures, *J. Biomechanics*, 41:200-207, 2008.

[8] Charpail E, Trosseille X, Petit P, Laporte S, Lavaste F, Vallancien G, Characterization of PHMS ribs: a new test methodology, *Stapp Car Crash Journal,* 49:1-16, 2005.

[9] Kindig M, Lau A, Kent R, Biomechanical response of ribs under quasistatic frontal loading, *Traffic Injury Prevention,* 12(4):377-387, 2011.

[10] Lau A, Oyen ML, Kent RW, Murakami D, Torigaki, T, Indentation stiffness of aging human costal cartilage, *Acta Biomaterialia*, 4:97-103, 2008.

[11] Forman J, del Pozo de Dios E, Arregui Dalmases C, Kent R, The contribution of the perichondrium to the structural mechanical behavior of the costal-cartilage*, J. Biomech. Engineering*, 132(9):094501, 2010.

[12] Holzapfel GA, Nonlinear Solid Mechanics: A continuum Approach for Engineering, *John Wiley & Sons*, 2000, England.

[13] Holzapfel GA and Gasser TC, A new constitutive framework for arterial wall mechanics and a comparative study of material models, *Journal of Elasticity,* 61:1-48, 2000.